J. Earth Syst. Sci. (2020)129 74
https://doi.org/10.1007/s12040-020-1342-z

Multi-approach synergic investigation between land surface temperature and land-use land-cover

Prasenjit Saha[1], Subhajit Bandopadhyay[2,*], Chandan Kumar[3] and Chandana Mitra[4]

[1]*National Atlas and Thematic Mapping Organization (NATMO), Kolkata, India.*
[2]*Laboratory of Bioclimatology, Department of Ecology and Environment Protection, Faculty of Environmental Engineering and Spatial Management, Poznan University of Life Sciences, Poznan, Poland.*
[3]*Department of Geological and Mining Engineering and Sciences, Michigan Technological University, Houghton, MI, USA.*
[4]*Department of Geoscience, Auburn University, Auburn, AL, USA.*
**Corresponding author. e-mail: subhajit.iirs@gmail.com*

MS received 15 July 2019; revised 13 November 2019; accepted 19 November 2019

Rapid urban expansion and associated land-use land-cover (LULC) change in India have emerged as a serious environmental threat that accelerates the impacts of urban heat island intensity (UHII). Three independent investigations have been conducted in this study using a series of Landsat data. The objectives of this work are: (1) To predict the near-future LULC scenario using an integrated model; (2) To understand the connection between band mean for particular LULC class with LST; (3) To analyze the temporal relationship between different types of built-up clusters and LST. The LULC and LST maps reveal that LST increases from 27.01° to 33.86°C, whereas built-up areas rise from 6.93% to 27.10% during 1988–2018, respectively. We observed that the near-future LULC scenario of KMA shows a huge expansion of built-up areas paid by decreased vegetation and open spaces. A clear significant correlation has been found between band mean and LST in all three Landsat sensors with the $R^2 = 0.84$; $p<0.02$ for Landsat 5 TM, $R^2 = 0.91$ and 0.99; $p<0.01$ and 0.00 for Landsat 7 ETM+, and $R^2 = 0.88$; $p<0.01$ for Landsat 8 OLI in connection to our second objective. However, no agreement has been found between different built-up clusters and LST over 30 years of observation. For the first time, this study established the interconnectivity between bands of Landsat sensors and LST. The temporal relationship between different built-up clusters and LST have reviled also for the first time. Beside this, the rising rate of built-up areas was observed by the integrated model. Such alarming condition demands immediate attention to sustainable, and scientific land use regulations under new urbanism policy.

Keywords. Land-use land-cover (LULC); land surface temperature (LST); urban heat island (UHI); Landsat; built-up clusters; India.

1. Introduction

Over the past few decades, global population growth and urban expansion have been acting as the primary drivers for transforming land-use land-cover (LULC) worldwide. This situation is common especially in underdeveloped and developing nations with an unstoppable desire for a prosperous economy (Lv and Zhou 2011). A developing nation like India has experienced a huge

Published online: 20 February 2020

population increase in recent decades. According to the last national census of 2011 report, the population was increased from 361 million in 1951 to 1,221 million in 2011 (James 2011; Moulds *et al.* 2018). Due to such a significant increase in population, an extreme change was observed in environmental and microclimatic systems in all major and minor cities of India. Urban migration, population pressure, and a dynamic economy all are reflected in the changing scenario of Indian cities (Kallvetty and Bandopadhyay 2018). The expansion of Indian cities encourages the transformation of natural land covers into impervious materials. Such transformations were made by biophysical environmental modifications, reduction in green paved spaces, compromised public space and parks and finally changes in the land surface energy process (Lo and Quattrochi 2003; Fu and Weng 2016; Pal and Ziaul 2017). These transformations have also influenced the absorption budget of solar radiation, heat storage, and transmission, local wind turbulence pattern, energy balance, water balance interactions, and normal environmental situations in direct or indirect ways (Oke 1987; Weng *et al.* 2004; Mallick *et al.* 2008). According to Chandler (1965) and Lombardo (1985), there are three prime adverse effects of urban heat island intensity (UHII) on a city: (1) decrease of evapotranspiration; (2) disturbance in the normal energy transformation process; (3) production of anthropogenic energy. These adverse effects ultimately enhance the land surface temperature (LST) concentration of urban centers. Thus the impact of urbanization on LST needs to be addressed through various approaches. The LST derived from satellite, airborne, unmanned automated vehicle (UAV) sensed thermal infrared (TIR) imageries are some of the key mechanisms which help to understand the impact of urbanization on LST (Fu and Weng 2016).

In literature, many studies have explored the nexus between LST, LULC, and UHI through various approaches. Studies have shown the general trend where the increasing rate of urbanization accelerates the LST concentration of urban centers (Yap 1975; Chen *et al.* 2006; Weng *et al.* 2006; Rinner and Hussain 2011). Chandra *et al.* (2018) have addressed that the LST concentration of Jaipur city (Rajasthan, India) was changing with the areal expansion of the city. The study has applied the buffer analysis of settlement expansion using temporal datasets of Landsat 5 TM and Landsat 8 OLI images. Based on the radial analysis, the outcome reviles that the areal increase of the urban areas accelerates the average temperature range (30°–35°C). However, the future expansion of urban areas and its impact on LST over Jaipur city was overlooked in this study. Kumar *et al.* (2018) have shown the temporal relationship between LST and different land cover types (vegetation, water bodies, barren land, etc.) using Landsat 5 TM and Landsat 8 OLI images. The study was conducted at the hilly terrain of Spiti valley (Himachal Pradesh, India). Although this study has shown the negative relation between vegetation cover (NDVI) and snow cover (NDSI) with LST through linear regression, the impact of urbanization on LST was not addressed. Seasonal and temporal diversity of LST according to the changing pattern of LULC units were studied by Pal and Ziaul (2017). The work was conducted over Malda town (West Bengal, India) using Landsat 5 TM and Landsat 8 OLI images. Supervised image classification technique with Mahalanobis distance in parametric rule used for LULC classification, whereas the fraction of vegetation cover over the study area was calculated through vegetation indices such as NDVI. The outcome showed that LST increases 0.070°C/year and 0.114°C/year during winter and summer periods where built-up areas were the highest contributor in LST concentration. In a different study, Hiremath *et al.* (2013) have investigated the LULC (particularly built-up and vegetation) and LST connection over 10 years in Bangalore city (Karnataka, India). The study has used Landsat TM images for LULC classification, whereas Landsat thermal bands were used to estimate LST. Post-supervised change detection analysis, as well as vegetation (NDVI) and built-up (NDBI) indices, were calculated to establish LULC and LST connection. Outcome reviles that LST values were increased on an average by 1.7°C and 2.2°C where built-up areas were the highest contributor in LST acceleration. Similar objective-based studies were conducted for other cities in India like Chennai (Rose and Devdas 2009), Mumbai (Grover and Singh 2015), Delhi (Mallick *et al.* 2008; Grover and Singh 2015), Kolkata (Sharma *et al.* 2015) using temporal satellite data.

Studies also showed the LULC and LST relationship through different approaches. Small (2006) showed that anomalies in urban thermal patterns were highly dependent on the modification of biophysical land surface components, evident from 24 global cities including Kolkata. The

study by Weng *et al.* (2004) have suggested that solar radiance, thermal, and moisture properties of the Earth surface have a direct relation to the LST of urban centers. Fu and Weng (2016) have proved that human-induced LULC modifications accelerated the surface thermal properties. The efficiency of Landsat images has been demonstrated by Lv and Zhou (2011) and Ibrahim and Rasul (2017) which shows impervious surfaces influencing the LST concentration in a city. Various methods (i.e., Bayesian average; linear consensus; logarithmic consensus; majority vote; fuzzy integral etc.) based classified LULC maps were also showed a significant positive co-relation with LST, examined by Du *et al.* (2014). So, most of the studies represented the LULC and LST nexus based on spatial or non-spatial modelling techniques using satellite data.

However, no such studies have focused on the future LULC scenario of the study area to understand the degree of urban expansion over time. This was also for the first time in the field of LULC and LST analysis, where bands of different Landsat imageries and its connection to LST were conducted. Furthermore, temporal analysis between different built-up clusters and LST were also studied for the first time in this domain. So in this study, a multi-approach investigation between LULC and LST, based on three different objectives, have been performed under a single umbrella. First, a predictive modelling of near-future LULC scenario was developed through an integrated model. In 1982, Walburg *et al.* (1982) introduced the spectral data (reflectance) as band mean in correspondence to Landsat Thematic Mapper (TM) bands (i.e., TM2 (520–600 nm), TM3 (630–690 nm), and TM4 (760–900 nm). Each band has taken with a sensor, which is sensitive towards a particular wavelength. We know that each surface or object of the earth interacts with incoming solar radiation in different ways. Incoming electromagnetic radiation, i.e., light can be absorbed, transmitted, emitted or reflected by such surface or object which is detected and captured by different wavelengths. Each LULC class (i.e., built-up, vegetation, waterbody, etc.) is highly sensitive to a particular wavelength detected by a particular band (example: NIR band for vegetation, blue band for water bodies, etc.). However, the connection between bands (spectral reflectance) responsible for particular LULC classes and its connection to LST was not analyzed yet. Filling this gap, in our second objective we have examined the relationship between LST and different Landsat bands responsible for different LULC classes. This analysis will help us to understand the sensitivity of different Landsat bands towards LST. Studies like Zha *et al.* (2003), Xiong *et al.* (2012), Chen *et al.* (2013) and Guo *et al.* (2015) have shown the general positive relation between built-up density and LST. But the temporal analysis between different built-up clusters and LST, have not been explored yet. Keeping this concern, the temporal relationship between different built-up clusters (i.e., highly dense, planned, slum and village) and LST have examined in our third objective. To the best of the authors knowledge, none of these objectives were examined for the cities of India particularly Kolkata within a single article.

The three objectives of this study are:

(1) To predict the near-future LULC scenario of the study area using an integrated model.
(2) To understand the connection between LST and Landsat bands responsible for different LULC classes.
(3) Temporal analysis between different built-up clusters with LST.

2. Study area

The study was conducted on the Kolkata Metropolitan Area (KMA) (figure 1), West Bengal, India. KMA experienced massive urban expansion in the past few decades (Bardhan *et al.* 2016). It is considered as the largest urban agglomeration of eastern India and the third-largest populous metropolitan following Delhi and Mumbai. Kolkata Metropolitan Development Authority (KMDA) is the responsible agency for planning, promoting and developing the KMA region.

KMA is situated at 22.329°–23.000°N latitude and 88.066°–88.556°E longitude. The geographical extension of KMA is spread over the 1886.67 km^2 area. This region is located in the lower deltaic plain of the Ganges–Brahmaputra–Meghna delta system where the main surface material is alluvial clay and clay loam (Bardhan *et al.* 2015).

KMA region comes under the tropical wet-and-dry climate zone with summer monsoons, fitted in the Koppen's climatic division of *Aw*. The mean monthly temperature in KMA ranges from 18° to 30°C and maximum temperatures can often exceed 40°C during May–June (Mitra 2018). Winter season begins from the last of November to early

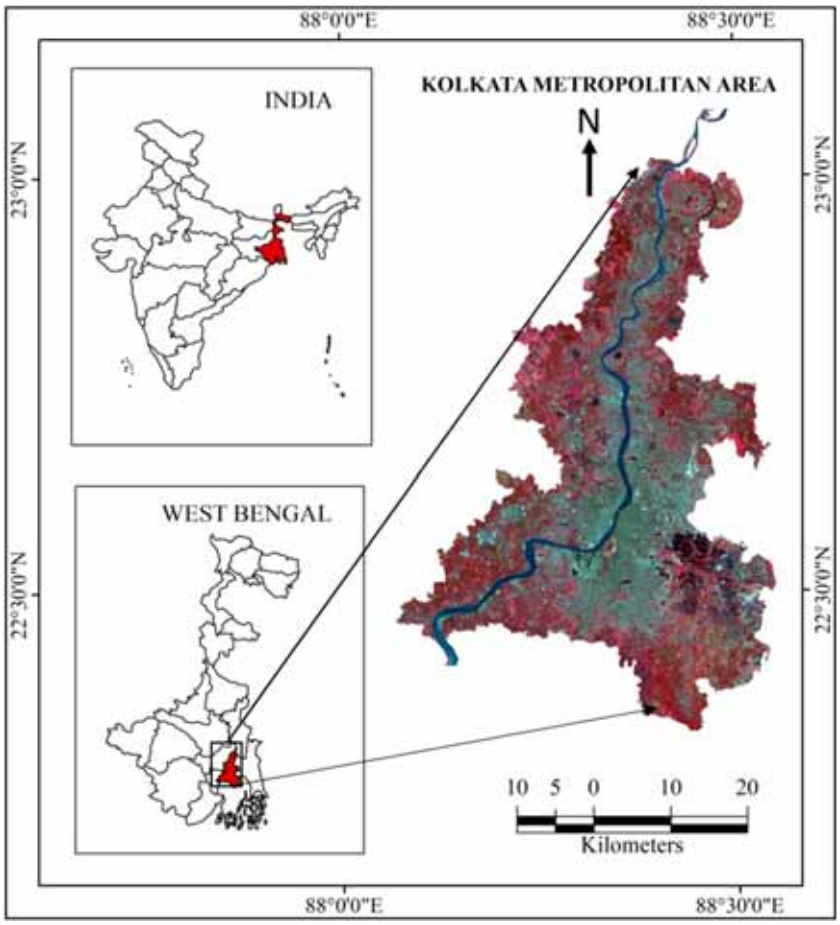

Figure 1. Location of Kolkata Metropolitan Area (KMA) in false colour composite (FCC) mode on Landsat 8 OLI image.

February, with the lowest temperatures hovering in the 12°–14°C during December and January. During summer, KMA and the other parts of West Bengal experience some locally developed thunderstorms known as Kalbaishakhi (Nor' wester). Like other parts of India, rainfall in this region is dominated by monsoonal precipitation from the end of June to the end of August (Chakraborty *et al.* 2019). The mean annual rainfall in this region is 1582 mm. Agriculture and industry both are the pillars of the economy in KMA. Due to unplanned urban expansion of Kolkata metropolitan, KMA suffers from poverty, excessive migration, increasing slum population, air pollution, traffic congestion and several socio-economic problems (Bhatta 2009; Ghosh *et al.* 2018).

3. Data and methods

3.1 *Datasets*

Three different sensors of Landsat series (i.e. Landsat 5 TM, Landsat 7 ETM+, and Landsat 8 OLI) have been used in this study. Landsat 5 TM for 1988, Landsat 7 ETM+ for 2000 and 2010, and Landsat 8 OLI for 2018 with an interval of 12, 10 and 8 years respectively, have been acquired freely from the US Geological Survey (USGS) Global Visualization Viewer platform (https://earthexplorer.usgs.gov/). The details of the acquired Landsat images are given in table 1(a, b, c). The obtained Landsat (level L1T) images were geometrically and topographically corrected. All the images were in Universal Transverse Mercator (UTM) projection system (zone 45 North for KMA) with WGS-84 datum. Necessary atmospheric corrections such as noise and haze correction have been performed on every image before mosaicking using ERDAS IMAGINE 2013 (Hexagon Geospatial., USA) and ENVI 5.3 (Harris Geospatial Solutions., USA).

3.2 *Methods*

The methodological framework adopted for individual objective was presented below.

Table 1(a). *Bands of Landsat 5 TM and its respective LULC class.*

Landsat 5 TM				
DOA: 26.12.1988		Datum and Projection = WGS 84 UTM Zone 45		ROW/PATH: 44 and 45/138
Band no.	Band name	Spectral range (μm)	Spatial resolution (m)	Sensitive class
1	Blue	0.450–0.515	30	Water
2	Green	0.525–0.605	30	NA
3	Red	0.630–0.690	30	NA
4	NIR	0.760–0.900	30	Vegetation
5	SWIR I	1.550–1.750	30	Urban and Industry
6	Thermal	10.40–12.5	120	LST
7	SWIR II	2.080–2.35	30	Open space

Table 1(b). *Bands of Landsat 7 ETM+ and its respective LULC class.*

Landsat 7 ETM+				
DOA: 26.01.2000 and 23.12.2010		Datum and Projection = WGS 84 UTM Zone 45		ROW/PATH: 44 and 45/138
Band no.	Band name	Spectral range (μm)	Spatial resolution (m)	Sensitive class
1	Blue	0.450–0.515	30	Water
2	Green	0.525–0.605	30	NA
3	Red	0.630–0.690	30	NA
4	NIR	0.760–0.900	30	Vegetation
5	SWIR I	1.550–1.750	30	Urban and Industry
6	Thermal	10.40–12.5	60 * (30)	LST
7	SWIR II	2.080–2.35	30	Open Space
8	Panchromatic	0.520-0.900	15	NA

Table 1(c). *Bands of Landsat 7 ETM+ and its respective LULC class.*

Landsat 8 OLI				
DOA: 11.01.2018		Datum and Projection = WGS 84 UTM Zone 4		ROW/PATH: 44 and 45/138
Band no.	Band name	Spectral range (μm)	Spatial resolution (m)	Sensitive class
1	Ultra Blue	0.435–0.451	30	NA
2	Blue	0.452–0.512	30	Water
3	Green	0.533–0.590	30	NA
4	Red	0.636–0.673	30	NA
5	NIR	0.851–0.879	30	Vegetation
6	SWIR I	1.566–1.651	30	Urban and Industry
7	SWIR II	2.107–2.294	30	Open Space
8	Panchromatic	0.503–0.676	15	NA
9	Cirrus	1.363–1.384	30	NA
10	TIRS I	10.60–11.19	100 * (30)	LST
11	TIRS II	11.50–12.51	100 * (30)	LST

*DOA: Date of image acquisition; NIR: Near Infrared; SWIR: Shortwave Infrared; TIRS: Thermal Infrared; NA: Not applicable in this study. Source: https://Landsat.usgs.gov/what-are-best-spectral-bands-use-my-study; https://Landsat.usgs.gov/what-are-band-designations-Landsat-satellites.

3.2.1 *LULC classification*

Four LULC maps of 1988, 2000, 2010, and 2018 were generated by the supervised classification technique with maximum likelihood (ML) approach using ERDAS IMAGINE 2013 (Hexagon Geospatial, USA). Several studies have adopted different classification techniques for LULC

mapping. For example, artificial neural network (ANN) by Erbek *et al.* (2004), support vector machine (SVM) by Chen *et al.* (2017a), object-based image classification by Drăguţand Blaschke (2006), Mahalanobis distance by Pal and Ziaul (2017) and so on. All of the mentioned classification techniques were highly dependent on the spatial heterogeneity or homogeneity of pixels. But specifically for urban LULC mapping where spatial heterogeneity of pixels is so high, the supervised classification based ML approach was extensively used and considered as an established technique in the literature (Sun *et al.* 2013; Sahana *et al.* 2018; Ghosh *et al.* 2018). The ML method is based on the relative class membership function (likelihood) including all train signature samples for each class in an image. ML approach needs the least computational time among other supervised classification algorithms such as minimum distance, Mahalanobis distance, etc. In comparison to the minimum distance, Mahalanobis distance, ML approach provides the best accurate classification outcomes, because it does not overestimate the class values during the computational process (Ahmadi and Hames 2009). The studies like Sun *et al.* (2013), Ahmadi and Hames (2009) and Erbek *et al.* (2004) have shown the strength of ML approach in comparison to other classification methods (i.e. minimum distance, Mahalanobis distance, ANN algorithms). The three main advantages of the ML approach are (1) allowing the reclassification process to reduce the error and improve the overall accuracy (Chen *et al.* 2017b). The post-classification correction technique within the ML classifier is allowing the user to refine the class assignment of a pixel after its initial classification (Thakkar *et al.* 2017). In this process, the post-classification correction technique first minimizes the number of misclassified pixels and further reclassify to assign misclassified pixels into its new class according to the spectral similarity. This process ultimately improves the overall accuracy of the classified image. (2) Auto-allocation of pixels to the unclassified regions based on the surrounding values (Ahmadi and Hames 2009). During the classification process, the unclassified pixels are assigned to a particular class based on the relative likelihood (probability) and spectral similarity of that pixel which is occurring within each class (Sun *et al.* 2013). This process repeats until each pixel assigned to a class and satisfies the spectral parameters. (3) Variance and covariance values of the class signatures are considered within the class distribution (Erbek *et al.* 2004; ERDAS 2009). It considers that the distribution of the class is normal and can be characterized by the mean vector and covariance matrix. Based on such considerations, the statistical probability is computed for each class to fix the assignment of a cell to the particular class.

The images of 1988, 2000, 2010, 2018 were classified into five major LULC classes, i.e., (i) built-up, covering the buildings and concrete areas, (ii) vegetation, covering the green vegetated areas, (iii) water bodies, covering the ponds, lakes, wetlands and major river system of the study area which is the Ganges, (iv) open space, covering the croplands and barren lands, (v) industry, covering the factories, workshops, and small to large size industries. In each class, 80 random samples (spectral signatures) have been taken from images for classification.

In the next stage, four generated LULC maps have been validated and authenticated using two techniques: (1) classified products were verified through Google Earth Engine, (2) accuracy assessment has been conducted. Details of the two mentioned steps were given below.

3.2.2 *Validation through Google Earth*

Four classified LULC maps were verified by Google Earth Engine at the first step (Luedeling and Buerkert 2008; Zhao *et al.* 2015). Google Earth uses very high-resolution images (e.g., QuickBird, IKONOS, SPOT5) of recent years at a spatial resolution of 1 m or so (Hu *et al.* 2013). Such high-resolution images help to distinguish different land cover types observed by the visual verification process. In our study, validation of four LULC maps using Google Earth Engine were conducted in ERDAS IMAGINE 2013 (Hexagon Geospatial, USA).

3.2.3 *Accuracy assessment*

In supervised classification, accuracy assessment was conducted through confusion or error matrix that allows differentiating between real and predicted classifications (Yuan 1997). All accuracy statistics, namely, overall accuracy (OA), user's accuracy (UA), producer's accuracy (PA) and kappa coefficient (k) were calculated for the four LULC maps. Equations for each accuracy statistics were given below.

$$\text{Overall accuracy (OA)} = \frac{\text{Total number of correct samples}}{\text{Total number of all samples}} \times 100\% \quad (1)$$

A total of 102 random sample sites has been selected automatically for OA assessment. The selection of 102 sample sites was an automated process by the software, i.e., ERDAS IMAGINE 2013. The sample sites were distributed equally over the whole study area.

Simultaneously, the classification accuracy within each class was also computed through UA and PA assessment using the following equitation:

$$\text{Comission . Error} = \frac{FP}{FP + TP} = \frac{FP}{\text{total predicted}}$$

So,

$$UA\,(\%) = 100\% - \text{error of commission}\,(\%) \quad (2)$$

$$\text{Omission. Error} = \frac{FN}{FN + TP} = \frac{FN}{\text{total reference}}$$

So,

$$PA\,(\%) = 100\% - \text{error of omission}\,(\%) \quad (3)$$

FP: false positive, *TP*: true positive, *FN*: false negative, and *TN*: true negative.

Furthermore, the kappa coefficient was calculated for each classified image. The purpose of calculating kappa coefficients was to measure the inter-observer agreement for classified items (Foody 1992). The equation for kappa coefficients (k) is given below:

$$k = \frac{n\sum_{k=1}^{q} n_{kk} - \sum_{k=1}^{q} n_{k+n_{+k}}}{n^2 - \sum_{k=1}^{n} n_{k+n_{+k}}} \quad (4)$$

here, n is the total number of pixels the ground or reference data, nkk is the total number of i class, nk is the total number of pixels for the ith class derived from the classified data, $n+k$ is the total number of pixels for the ith class derived from the reference data, q is the total number of class (Ghosh *et al.* 2018). In simple terms, the above equation stands like:

$$k = \frac{(\text{Total} * \text{Sum of correct}) - \text{Sum of all the}\,(\text{row total} * \text{column total})}{\text{total squared} - \text{Sum of the all the}\,(\text{row total} * \text{column total})} \quad (5)$$

The kappa value *(k)* is always less than or equal to 1. The k value ranges from 0.70 to 0.85 considered as very high accuracy, and >0.85 is considered as outstanding accuracy of the classified map (Monserud and Leemans 1992).

3.3 *LST retrieval from satellite images*

Advancement of thermal remote sensing has allowed us to develop several algorithms for LST retrieval from Landsat images. For example, radiative transfer algorithm (Sobrino *et al.* 2004), mono-window algorithm (Qin *et al.* 2001), single-channel algorithm (Jiménez-Muñoz and Sobrino 2003) and so on. However, it is challenging to obtain real-time atmospheric profile data during satellite overpass, which is an important requirement for the mentioned algorithms (Shen *et al.* 2016). But a good LST retrieval algorithm should have the ability to derive surface temperature independently that provides a high level of accuracy. Therefore, in this study, the mono-window algorithm developed by Qin *et al.* (2001) has been applied to retrieve LST from the four Landsat images. The mono-window algorithm needs only two atmospheric parameters compared to other retrieval algorithms. First, transmittance and second, mean atmospheric temperature (Qin *et al.* 2001; Lv and Zhou 2011).

The thermal band 6 of Landsat 5 TM, thermal band 6 of Landsat 7 ETM+ and the mean of thermal bands 10 and 11 of LANDSAT 8 OLI with a spatial resolution of 120, 60, and 100 m, respectively have been used in this study for LST retrieval using the mono-window algorithm.

Following steps were adopted for LST retrieval:

3.3.1 *Conversion of digital number (DN) to spectral radiance (Lλ)*

The conversion of DN number to spectral radiance ($L\lambda$) is based on simple electromagnetic principle. Every object in earth emits its thermal electromagnetic radiation after its temperature is above absolute zero (K). Based on this principle, the signal received by the different thermal sensors (TM, ETM+, TIRS) can be transferred to at-sensor radiation using the following equation:

$$L\,(\lambda) = \text{gain} * \text{QCAL} + \text{offset} \quad (6)$$

In the simplest way, it can describe like,

$$L(\lambda) = \frac{\text{LMAX} - \text{LMIN}}{255} * \text{DN} + \text{LMI} \quad (7)$$

where, $L(\lambda)$ = spectral radiance $\text{w}\cdot\text{sr}^{-1}\cdot\text{m}^{-3}$; LMIN = 1.238 (spectral radiance of DN value 1); LMAX = 15.600 (spectral radiance of DN value 255); and DN = digital number.

3.3.2 *Conversion of spectral radiance (Lλ) to satellite brightness temperature in Kelvin*

In this segment, the spectral radiance values *(Lλ)* of the Landsat thermal bands were converted to at-sensor brightness temperatures, with the assumption of uniform emissivity (equation 8) (Chander *et al.* 2009).

$$T_B = \frac{K_2}{\ln\left(\frac{K_1}{L_\lambda} + 1\right)} \quad (8)$$

where T_B = At-satellite brightness temperature (K); $L\lambda$ = spectral radiance in $\text{W.m}^{-2}.\text{sr}^{-1}.\mu\text{m}^{-1}$; K_1 and K_2 = K_1 and K_2 are two pre-launch calibration constants (Landsat-5 TM: K_1 is 607.76 $\text{W}/(\text{m}^2\text{sr}\mu\text{m})$ and K_2 is 1260.56 K; Landsat 7 ETM+: K_1 is 666.09 $\text{W}/(\text{m}^2$ sr μm) and K_2 is 1282.71 K; and Landsat-8 TIRS: K_1 is 774.89 $\text{W}/(\text{m}^2$ sr μm) and K_2 is 1321.08.[1]

3.3.3 *LST estimation*

The obtained values of T_B or T_{sensor} were referenced as a black body, which is quite different from the properties of real objects on the Earth's surface (Shen *et al.* 2016). Therefore, it was necessary to rectify the spectral emissivity. Finally, the LST from T_B values have been computed based on the following equation (Artis and Carnahan 1982):

$$LST = T_B/(1 + \{(\lambda \times T_B/\rho\varepsilon)\}) \quad (9)$$

where, LST is in Kelvin; T_B is the black body temperature and also the satellite brightness temperature in Kelvin; λ is the wavelength of the emitted radiance in meters; $\rho = h \times c/\sigma$ (1.438×10^{-2}m K); σ = Boltzmann constant (1.38×10^{-23} J/K); h = Planck's constant (6.626×10^{-34} J s); c = velocity of light (2.998×108 m/s) and ε = emissivity (ranges between 0 and 1).

Finally, LST temperature retrieved in Kelvin have been converted to degree Celsius using the following formula:

$$T_{LST} = T_B - 273. \quad (10)$$

3.4 *Comparison of derived LULC and LST*

Four LULC and LST maps of 1988, 2000, 2010, and 2018 were further analyzed to achieve the three objectives of this study (see figure 2).

3.4.1 *Predictive modelling using integrated CA–Markov chain model*

Predicated LULC scenario for 2026 of KMA has developed through integrated cellular automata (CA)– Markov chain model.

The efficiency and accountability of the Markov chain in land-use change modelling is promising and well-established. Markov chain has its capability to quantify not only the states of alteration between land-use types but also able to quantify the rate of conversion within the land-use types (Sang *et al.* 2011; Kallvetty and Bandopadhyay 2018). The best part of this model is that the Markovian model estimates the quantity of change and the CA model geographically evaluates this spatial change (Hamad *et al.* 2018). CA–Markov is a hybrid modelling approach that includes the deterministic modelling framework, spatially explicit approach with a stochastically based temporal framework (Keshtkar and Voigt 2016). Studies found that combination of CA and Markov model were working quite good as an operational model in comparison to other LULC prediction models such as multi-layer Perceptron–Markov Chain (MLP-MC), GEOMOD, etc. (Regmi *et al.* 2014). CA–Markov allows the user to add many factors into the model to improve the accuracy and it serves land-use planners and policy makers in order to frame correct decisions on future land use policy (Hamad *et al.* 2018). As this study outcome incorporates the LULC and LST together which will help planners and policy makers to develop sustainable land use policy in the coming future, we found the CA–Markov model would be suitable for this study.

Earlier Markov model has been extensively used in ecological modelling. But further, this model was accepted by other predictive modelling studies (for example LULC change modelling) (Brown *et al.* 2000). The Markovian simulation is quite significant in the space–time consortium. In this model, the state of a system at the time t_2 can be predicted, at the time of t_1 within a spatial domain

[1] Source: http://Landsat.usgs.gov/Landsat8_Using_Product.php.

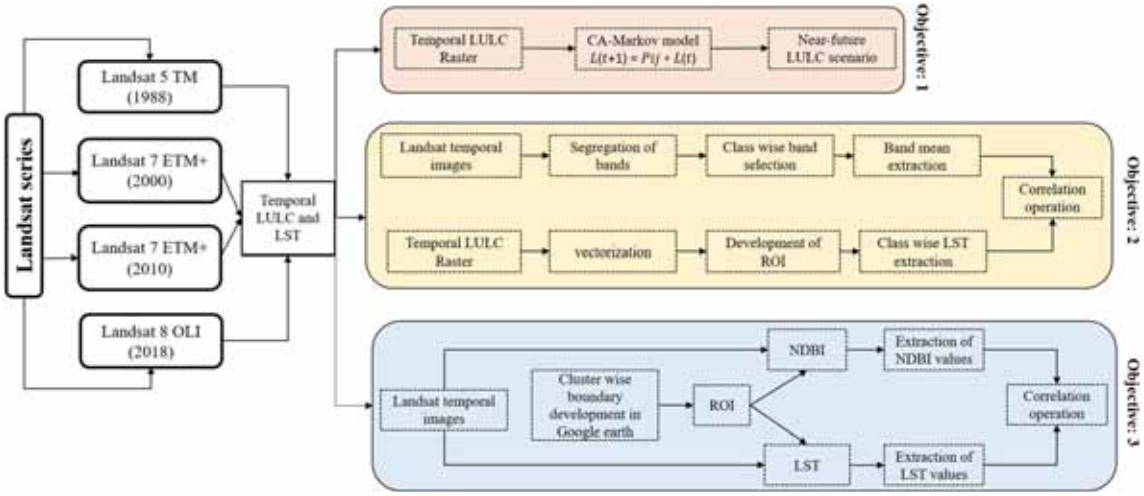

Figure 2. The methodological framework adopted in this study with objectives.

(Thomas and Laurence 2006). The Markovian simulation is based on the transition area matrix, which is obtained from the transition probability matrix. The transition probability matrix expresses the likelihood that a pixel of a given class will alter to any other class (or stay the same class) in the future time period (Behera *et al.* 2012).

Markov chain integrates with CA and used for the predictive modelling of LULC change (Sang *et al.* 2011). The reason behind this integration was not only spatial contiguity but also to identify the probable spatial transactions occurring over time in a particular spatial context. In this process, the generated change map and associated transition area matrix are required which is used as a base for future LULC prediction. A number of CA iterations have been conducted between input parameters. A single iteration or the cycle of iterations are the gaps between two input images.

In our study, we have predicted the LULC scenario of KMA for the year 2026 based on the LULC maps of 2010 and 2018 with one iteration of 8 year. CA-Markov model for predicting land-use change can be represented mathematically as an equation (12).

$$L_{(t+1)} = P_{ij} * L_{(t)} \tag{12}$$

and

$$\begin{bmatrix} P_{11} & P_{12} & \ldots P_n \\ P_{21} & P_{22} & \ldots P_n \\ P_{n1} & P_{n2} & \ldots P_{nn} \end{bmatrix}$$

where $L_{(t+1)}$ and $L_{(t)}$ are the land-use status at time t+1 and respectively.

$\left\{0 \leq P_{ij} < 1 \text{ and } \sum_{j=1}^{m} P_{ij} = 1(i, j = 1, 2 \ldots, m)\right\}$ is the transition probability matrix in a state.

3.4.2 *Band mean extraction and connection to LST*

Every object on the Earth's surface is sensitive or responsive towards a particular wavelength. The sensitivity of an object is captured by a particular band of the image. For example, vegetation on the surface is highly responsive to the NIR band, water bodies are highly responsive to the blue band, urban and concrete areas are responsive to the SWIR I band and so on. The detailed list of responsive bands and their respective LULC classes (objects) for three Landsat sensors (e.g., Landsat 5 TM, Landsat 7 ETM+, and Landsat 8 OLI) are given in table 1(a, b and c).

To understand the relationship between the sensitive band of particular LULC class and LST, first, we have calculated the mean of each and every band for three different Landsat sensors. We have conducted this analysis for all three Landsat sensors to avoid any biased outcome for a particular Landsat senor.

Simultaneously, we have retrieved the mean LST value for each LULC class for four consecutive years. Furthermore, year-wise linear regression has been performed between the mean LST values of each LULC class and the mean band values of each LULC class.

3.4.3 *Cluster analysis and connection to LST*

In this segment, the relationship between the built-up density of different types of built-up clusters and LST have been performed for four consecutive years. The density of four types of built-up clusters (i.e., highly dense, planned, slum pockets, and

village) has been calculated from Normalized Difference Built-up Index (NDBI).

3.4.3.1 *Development of NDBI:* To aim towards automated mapping of built-up areas and impervious surfaces from satellite imagery, Zha *et al.* (2003) proposed the concept of NDBI. Presently, NDBI is the most commonly used and widely accepted technique for the identification of built-up areas and its density (Zha *et al.* 2003). Built-up areas are sensitive under 1.55–1.75 μm wavelength range recorded in middle infrared (MIR) band or in the SWIR band, whereas low sensitivity of built-up areas is observed under 0.76–0.90 μm wavelength range, recorded in near-infrared (NIR) band (Bhatti and Tripathi 2014).

The NDBI equation is:

$$\mathrm{NDBI} = \frac{\mathrm{SWIR} - \mathrm{NIR}}{\mathrm{SWIR} + \mathrm{NIR}} \tag{11}$$

The NDBI values generally range from –1 to +1. The values close to –1 represents non-built-up areas such as water body, vegetation, and the values close to +1 represents highly dense built-up clusters. For Landsat TM, ETM+, and OLI, SWIR band stands in band 5, whereas for Landsat TM and ETM+, NIR band stands in band 4. For OLI, NIR band stands in band 5 (Ghosh *et al.* 2018). So, following the equation (11), we have derived the NDBI maps of the KMA region for four consecutive years.

3.4.3.2 *Selection of different built-up clusters and correlation to LST:* Four different categories of built-up clusters have been selected for this analysis based on prior knowledge of the study area. Selected built-up clusters were (i) highly dense, (ii) planned, (iii) slum pockets and (iv) village. The boundaries of four built-up clusters have been demarcated from the Google earth engine (Xia *et al.* 2019). The analysis considered, 2 boundaries of a highly dense cluster, 2 boundaries of the planned cluster, 12 boundaries of slum pockets, and 5 village boundaries. Furthermore, the boundaries were converted to a region of interest (ROI) file to extract the NDBI values of built-up clusters. The mean NDBI value of four built-up clusters has been considered for the final analysis. Figure 3 shows the close view of four types of built-up clusters at the KMA region.

Simultaneously, the mean LST values have been retrieved using the same ROI files of built-up clusters. Finally, linear regression has been conducted to understand the relationship between different built-up categories and LST for four consecutive years (1988, 2000, 2010, and 2018).

4. Results

4.1 *Temporal LULC analysis*

The LULC maps of the KMA region for the years 1988, 2000, 2010, and 2018 have been shown in figure 4.

Along with the visual validation of four LULC maps through Google earth, the kappa values, PA, UA, and OA assessment results are given in table 2. The satisfactory OA and kappa values have shown the authenticity of LULC maps in all 4 years.

It was observed that built-up areas of KMA had increased over time whereas vegetation and open space areas had significantly declined (see figure 5). The built-up areas had increased from 6.93% in 1988, 10.37% in 2000, and 16.05% in 2010 to 27.10% in 2018. The highest built-up growth was taking place between 2010 and 2018 at the rate of 11.05%. Vegetation covers were drastically decreased over time at the rate of 15.62%, 8.56%, 5.48%, and 2.03% for the years 1988, 2000, 2010, and 2018, respectively. Similarly, open spaces were also reduced from 74.54% in 1988 to 68.28% in 2018. However, a negative trend has been observed after 2000 in the industrial class. Fluctuations have been observed for water bodies during 1988–2018.

4.2 *Temporal LST analysis*

LST maps of 1988, 2000. 2010, and 2018 have shown the spatial variation in surface temperature. During 1988, the LST values were ranging from 16.85° to 27.01°C. During 2000 and 2010, the LST values were ranging from 17.10° to 30.20°C and 17.50° to 29.70°C, respectively. The highest temperature gap was recorded during 2018, where the LST values were ranging from 19.90° to 33.86°C. Except for 2010, all other years have clearly shown an increase in mean LST values, ranging from 5° to 7.25°C (figure 6).

4.3 *Outcome of predictive modelling*

The near-future LULC scenario of the KMA region for the year 2026 has been shown in figure 7. From figure 7, it is clear that the whole KMA region will

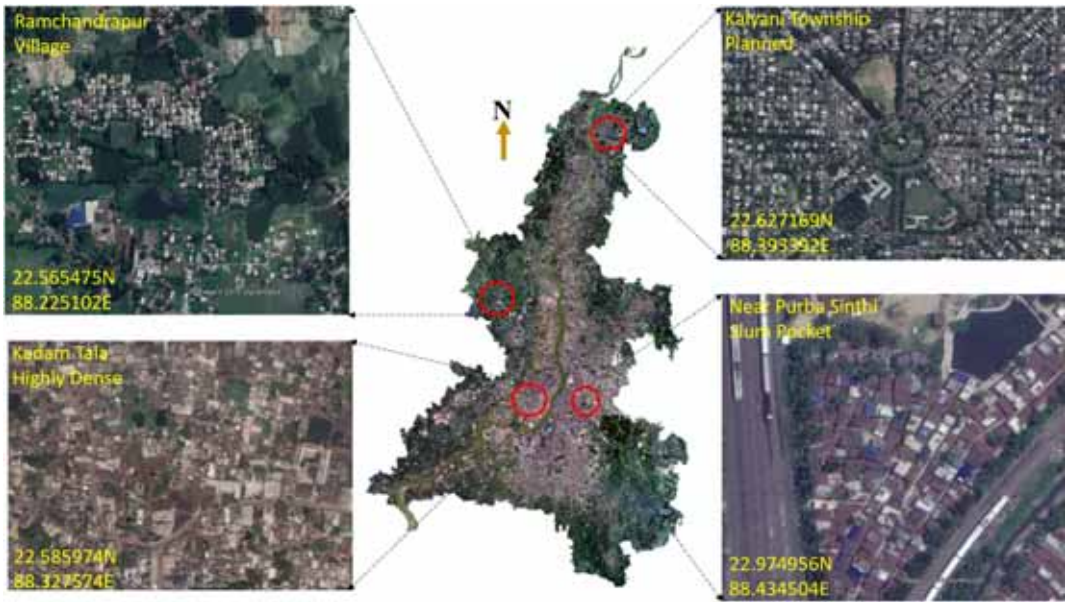

Figure 3. Location of highly dense, planned, slum pocket and village clusters (one each) on Google earth image (*Image courtesy Google earth*).

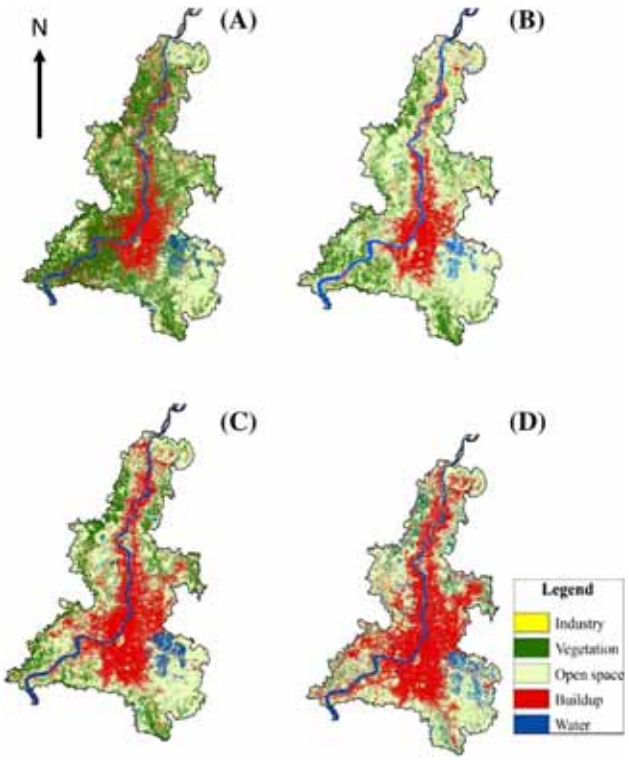

Figure 4. LULC maps of KMA for the year **(a)** 1988, **(b)** 2000, **(c)** 2010, and **(d)** 2018.

be filled with built-up areas whereas open spaces and vegetation covers will be reduced in a significant way.

The modelled outcome of near-future LULC scenario showed that in 2026 built-up areas will increase to 34.08% from 26.12% in 2018. Such an increase has shown a positive gain in built-up areas at the rate of +7.96% in 8 years (see figure 8). However, open spaces will be decreased to 60.41% from 68.28% with a negative rate of –7.87. No such significant change has been noticed in vegetation cover during 2026. It was predicted that the vegetation will cover 1.87% area of total KMA in 2026. Predictive modelling of 2026 showed that water bodies and industry will increase to 3.52% and 0.12% respectively from 2018 may be due to water conservation and industrial policy reforms.

4.4 *Band Mean and LST relationship*

The band means for sensitive LULC class have shown a significant and strong agreement with its respective LST for all three Landsat sensors (figure 9).

The band means and LST of respective LULC classes have shown a significant (p<0.02) and a strong correlation with the R^2 of 0.84 for the Landsat 5 TM sensor in 1988. The band mean value of SWIR I (sensitive to urban and industry class) has associated with the highest LST values. The SWIR II band mean value (sensitive to open spaces) is associated with moderate LST values, whereas blue and NIR band (sensitive to water and vegetation respectively) are associated with low LST values. Similarly, for Landsat 7 ETM+ sensor, the band means and LST of respective classes have shown significant (p<0.01 and p<0.00) and strong correlations with R^2 of 0.91 and 0.99 for 2000 and 2010, respectively. The band mean of SWIR I

Table 2. *Calculated kappa values, PA, UA and OA results of all four LULC maps.*

	UA					PA						
Year	I	V	OS	B	W	I	V	OS	B	W	OA	KAPPA
1988	95.25	83.33	90.00	80.04	92.31	82.11	90.91	91.77	72.76	88.61	86.87	0.82
2000	91.56	93.75	80.06	94.74	90.26	87.95	88.24	94.35	81.82	83.33	87.78	0.84
2010	98.37	90.01	91.30	95.36	95.88	83.70	94.74	87.50	94.12	93.42	89.06	0.87
2018	92.20	98.30	70.01	75.00	90.00	86.30	90.23	70.00	85.71	94.74	85.94	0.81

*UA: User accuracy; PA: Producers accuracy; OA: Overall accuracy; I: Industry; V: Vegetation; OS: Open space; B: Built-up; W: Water.

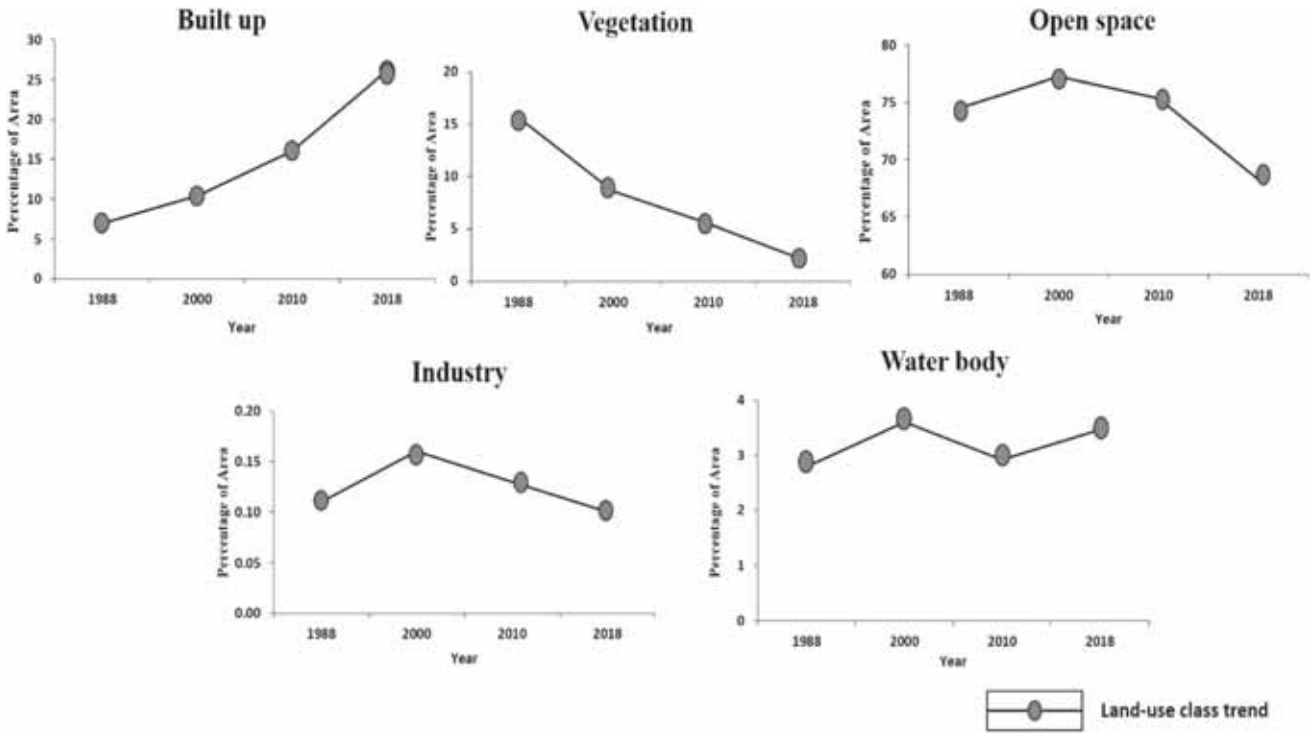

Figure 5. showing year wise percentage of areal change in individual land use class computed from LULC images.

(sensitive to urban and industry class) has associated with the highest LST values in both years. For the years 2000 and 2010, SWIR II (sensitive to open spaces) has linked with moderate LST values. Water and vegetation classes which are sensitive to blue and NIR band respectively, have associated with low LST values in both of years. No such difference in the relation between band means and LST has been found for Landsat 8 OLI sensor in 2018. A significant (p<0.01) and strong agreement (R^2 = 0.88) has been found between band mean values and LST for Landsat 8 OLI sensor. Urban and industry classes that were sensitive to SWIR I band have associated with the highest LST values whereas SWIR II band which was sensitive to open spaces has linked with moderate LST values. In a similar connection to TM and ETM+ sensors, blue and NIR band means (sensitive to water and vegetation respectively) have associated with low LST values.

4.5 *Different built-up clusters and LST relationship*

Temporal analysis of built-up density (represented by NDBI) for four types of clusters (i.e., highly-dense, planned, slum pockets, village) and its connection to LST have been delivered in this section. Figure 10 has shown the variations in NDBI concentration from 1988 to 2018 for different built-up clusters. NDBI, which was represented as an indicator of built-up density, has shown an increasing trend of 0.78 to 0.92 for the highly dense built-up cluster from 1988 to 2018. Similarly, the built-up density for the planned zone has also increased from 0.59 to 0.83 over the last 30 years.

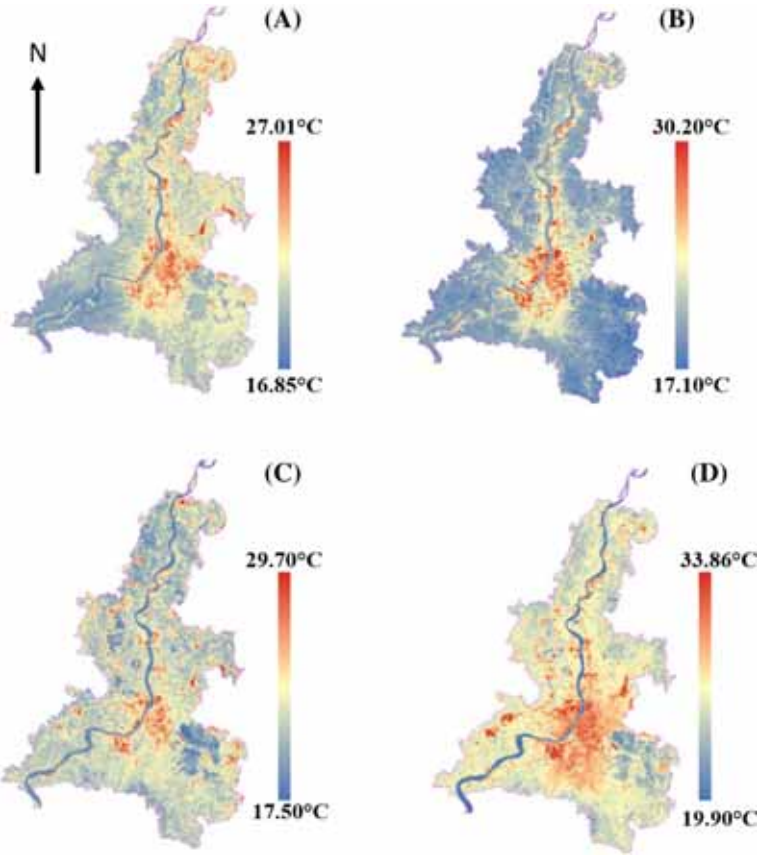

Figure 6. LST maps of KMA of the years **(a)** 1988, **(b)** 2000, **(c)** 2010, and **(d)** 2018.

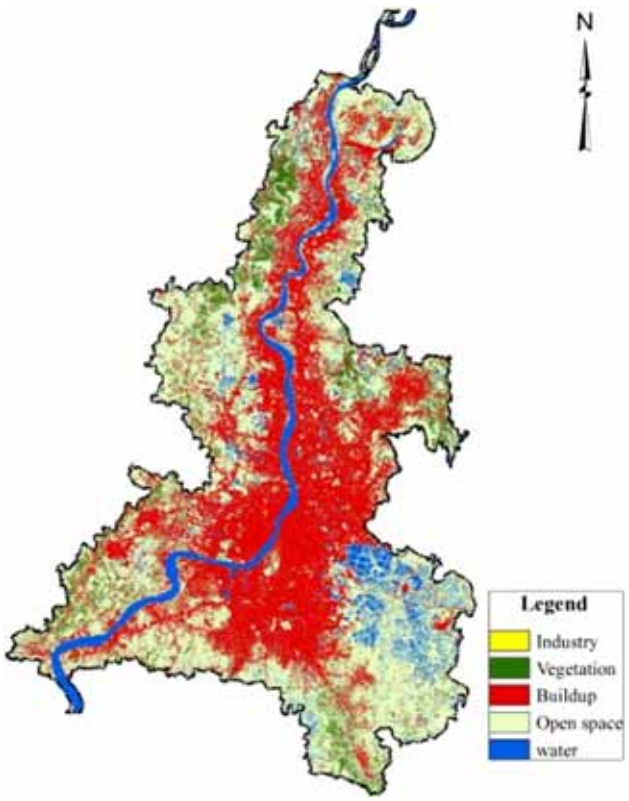

Figure 7. Predicted LULC map of KMA for 2026.

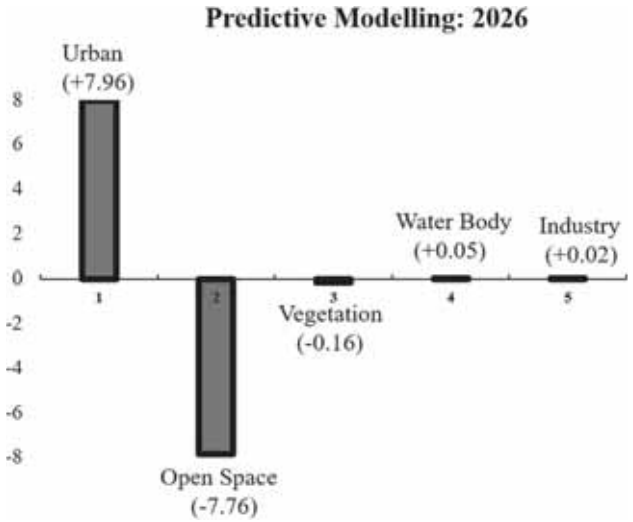

Figure 8. Quantitative representation of class-wise land use change in 2026 computed from the predicted LULC map.

No such trend but fluctuations have been found for slum pockets from 1988 to 2018. During 1988 NDBI for slum pockets was 0.88 and then it was declined to 0.75 in 2010. But NDBI for slum pockets was increased again to 0.88 during 2018. However, the built-up density for the village cluster has shown

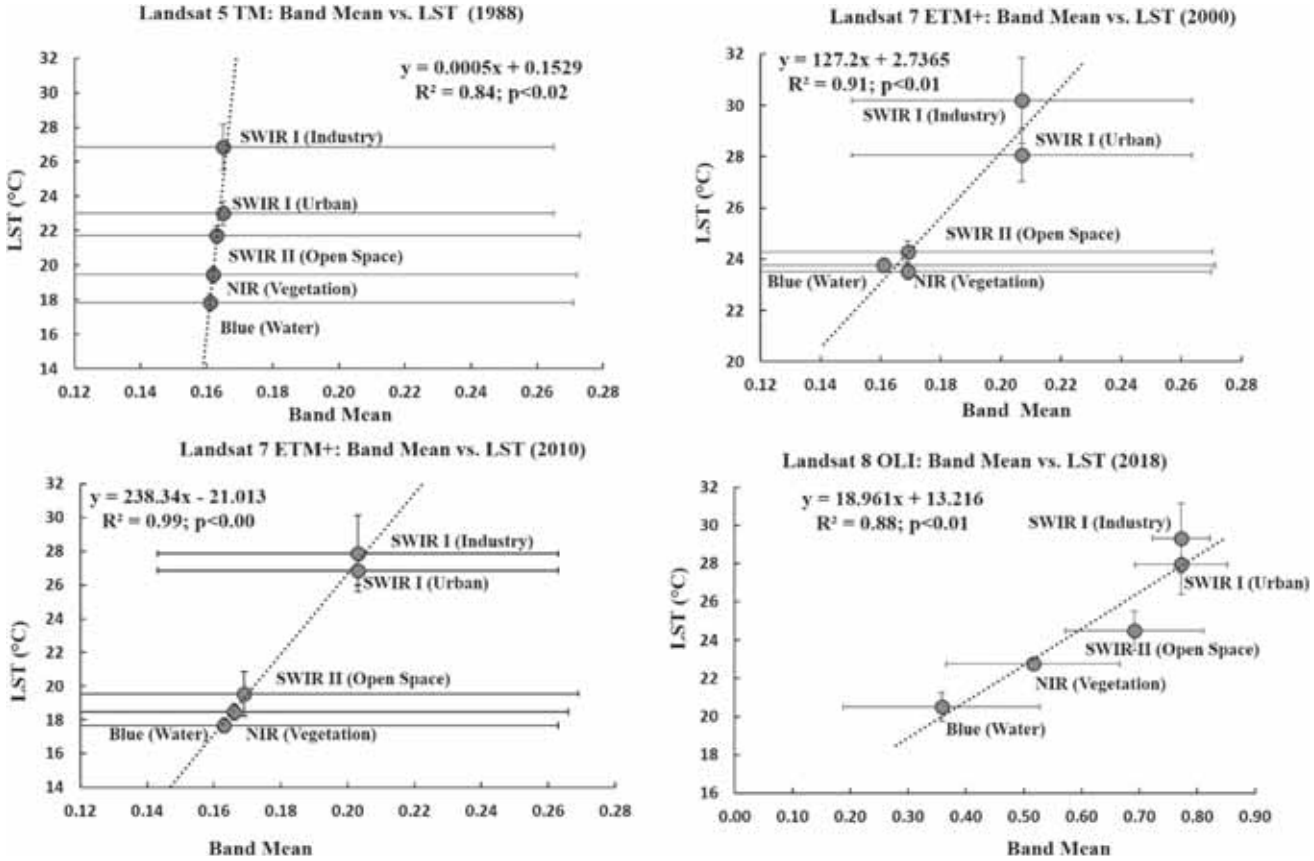

Figure 9. Relationship between band means for sensitive LULC class and its respective LST.

an increasing trend from 0.49 from 1988 to 0.72 during 2018.

Although there was a clear increasing trend of NDBI in all four built-up clusters from 1988 to 2018, no such significant relationship have been found between NDBI and LST (figure 11). A positive trend with an insignificant correlation (p<0.37; R^2=0.38) has been found between NDBI and LST for the highly-dense built-up cluster from 1988 to 2018. During the same period of time, built-up clusters like planned zone and slum pocket were also shown a positive insignificant correlation between NDBI and LST with p<0.35; R^2=0.41 and p<0.24; R^2=0.57, respectively. Poor agreement between NDBI and LST has been found for the village cluster with R^2 of 0.24 and p<0.50 during the observation period.

5. Discussion

5.1 *Temporal LULC and LST change*

The present study has reported a synergetic analysis between LULC change and its connection to surface thermal properties using a temporal series of Landsat imageries during 1988–2018. In comparison with previous studies on Kolkata (Kolkata Municipal Corporation) and KMA region (Ghosh *et al.* 2014; Bhattacharjee and Ghosh 2015; Sharma *et al.* 2015; Li *et al.* 2016; Mondal *et al.* 2017; Sharma 2017) the present study has shown three novel approaches that established the inter-connection between LULC change and LST, which were never done before.

Results derived from four validated LULC maps of KMA have shown huge urban expansion paid by decreasing vegetation cover and open spaces from 1988–2018. The study reports an overall accuracy in the range of 85%–90% for LULC classification and mapping (see table 2). This spatial expansion of built-up areas in KMA was the consequence of increasing urban population pressure (Sharma *et al.* 2015). There were two main reasons behind this increasing urban population pressure: firstly, Kolkata is the prime metro city in eastern India, so that enormous local and national migration took place in KMA for employment and business opportunities, to change the mode of living, social

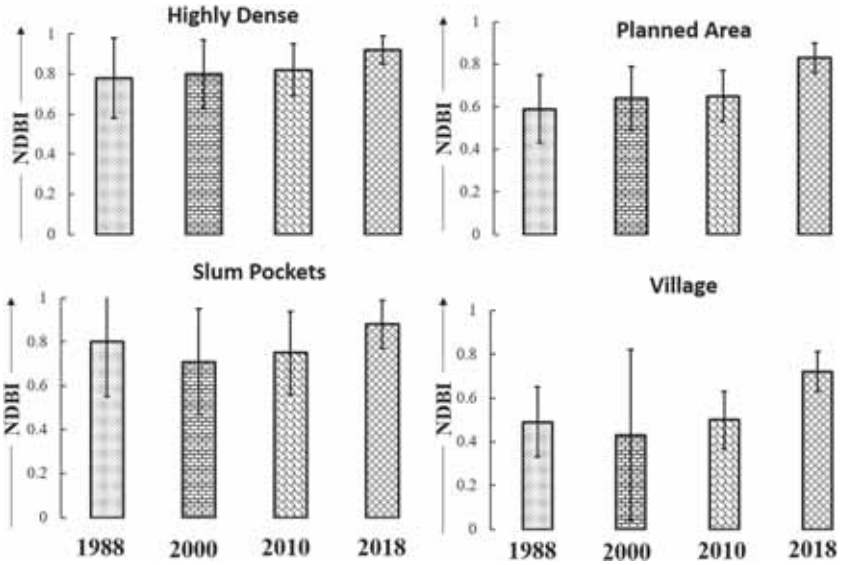

Figure 10. Temporal representation of NDBI values of four built-up clusters.

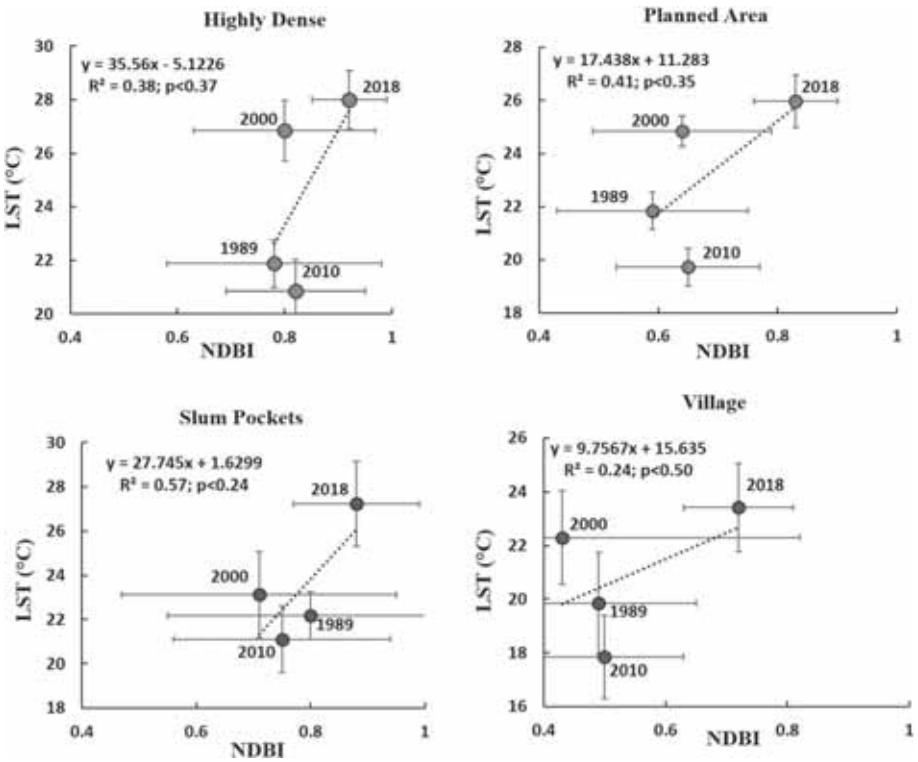

Figure 11. Relationship between NDBI and LST during 1988 to 2018 for different built-up clusters.

benefits, services, and administrative purposes, etc. Secondly, rural–urban transformation (McGee 2008) where the surrounding village and rural areas around KMA were transformed into urban centers and increasing the population pressure. Studies conducted by Mitra (2002), Roy *et al.* (2004), Mukherjee (2015), Sharma (2017) reported this progress as unplanned and haphazard development. Such unhealthy transformation was influencing the LST concentration of the KMA region over time, which was also visible in our study. The decreasing vegetation cover over time will seriously affect KMA's ecological integrity and alter its micro-climate scenario (Ghosh *et al.* 2014). Such condition demands serious mitigation measures in a form of social forestry, afforestation,

improving health and water status, and so on. A few mitigation measures have been taken over time, but our result shows that the city is far behind in achieving the goals. The loss of vegetation cover and open spaces with huge urban expansion was extremely worrying as it was significantly increasing LST over the KMA region, which was also evident from our results. The average gap between maximum and minimum LST in this region have increased from 10° to 14°C within the last 30 years, as a serious matter of concern. The major causes behind such an increase in LST concentration over 30 years were, first the modification of the land surfaces that includes built-up expansion, reduction of vegetation and water bodies, and rapid decline of open spaces. Second, the shape and positioning of buildings restricted the regular air movement near the ground surface. It creates complex shades of sunlight penetration and such complex pattern of shades limiting the natural energy exchanges. Third, the uncontrolled emission of waste heat from workshops, small and big industries, transportations, dumping sites also accelerate the LST concentration of the KMA area. Finally, the continuous emission of greenhouse gases (GHGs) such as carbon dioxide (CO_2), methane (CH_4), nitrous oxide (N_2O), and several others have also played a vital role to support these increasing warming scenarios.

The LST maps have shown the spatial variability of surface temperature over the KMA region. The maximum LST have found along the bank of river Hooghly particularly at the northern and south-western part of KMA. Those parts of KMA were characterized by high built-up concentrations. Not only that, the northern portion of KMA was the oldest part of this region, where residential, commercial buildings were developed in an unplanned way with a less green cover and few water bodies. The LST was in its peak in the northern and south-western parts of KMA due to the high absorption of solar radiation by the buildings. The building rooftop materials in these parts were mostly in concrete and have closely spaced buildings. Such kind of rooftop materials has a high potentiality to retain solar radiation with less reflection. Therefore, the materials were released more thermal energy in the local environment which was sufficient to develop the localized UHII (Sadhu 2015). The southern part of KMA was relatively new and planned in KMA. Sufficient vegetation cover and water bodies reduced the LST concentration in this part. The village areas were located on the outskirts of the KMA boundary and they were less influenced by LST due to less concretization, high green cover and a sufficient number of water bodies.

Thus the overall scenario of LST during 1988–2018 has shown an enhancement of thermal intensity in the KMA region due to built-up expansion and decreasing vegetation cover.

5.2 *Analysis of predictive modelling*

The application of the integrated model that combines the Markov chain and CA together has proved its potentiality to predict the near-future LULC scenario of the study area. Verified inputs (i.e., 2010 and 2018 LULC maps) and the CA–Markov chain model have successfully simulated the LULC scenario of KMA for 2026. This study applies, the original data resolution of Landsat (30 m), established administrative boundary of KMA (1988–2018), smallest possible scale for mapping, and assumed that in near-future the administrate boundary of KMA will not modify (at least till 2026). So, we consider the effects of modifiable areal unit problem (MAUP) to be ruled out and therefore MAUP has no role in our CA–Markov based predictive modelling (Campagna *et al.* 2012; Bojesen *et al.* 2015). Similarly, the temporal counterpart of MAUP which is modifiable temporal unit problem (MTUP) was also omitted from this model as we have used temporally adjusted intervals (2010 and 2018) as input for this model and also no segmentation and zoning of KMA boundary was performed to get the near-future LULC scenario in 2026 (Cheng and Adepeju 2014).

To our knowledge, this was the first time when the integrated CA–Markov chain model was applied over the whole KMA region to predict the near-future LULC scenario. Predicted LULC map has proposed a continuous rise in built-up with a serious decrease in vegetation cover and open spaces. We can assume that this scenario will continue for the next consecutive years. The rapid shrink of open spaces which also includes croplands is really a matter of concern in such a situation with an increasing population and high demand for food and water. Similarly, decreasing vegetation is more of a concern from an environmental and ecological perspective. Therefore, it is urgent to strengthen the protection of croplands, water

bodies, and vegetation covers, to prevent acts against the indiscriminate use of lands (Sarkar *et al.* 2016).

5.3 *Sensitivity of band means to LST*

We have found statistically significant and strong positive agreement between band means of sensitive LULC classes and its respective LSTs for three different Landsat sensors. This analysis opened a new window to establish the interconnection between LULC and LST. We have observed that blue band mean which was sensitive to water class was associated with low LST whereas SWIR I band mean which was sensitive to urban and industry classes were associated with high LST. A similar condition was found for other bands also where we found NIR and SWIR II band means were associated with low and moderate LST respectively. The overall scenario was exactly similar for all three Landsat sensors. Thus we can assume that the responsible band of a particular LULC class was sensitive to the respective LST.

In the LST derivation model (mono-window algorithm) adopted for this study, emissivity (ε) obtained from different LULC classes plays a crucial role here (see equation 9). Snyder *et al.* (1998) have mentioned that the spectral property of a particular object on the Earth's surface was highly sensitive to emissivity. The object at a temperature above absolute zero emits thermal radiation which was detectable and sensitive to a particular wavelength (recorded as a band). The emissivity of the object made by a particular matter was not only depending on the material but also on the nature of the surface (Honnerová *et al.* 2017). Apart from the surface and material of the object, the emissivity of the target was also depending on many other factors such as chemical composition, structure, roughness, and water content. For vegetation, low areal density and growth state were impacting towards low emissivity whereas impervious surfaces like urban and industrial class, have high built-up concentration and concrete material that were influencing towards high emissivity. Thus it was possible to predict the LST scenario of any LULC class from the band mean of that particular class. This relationship between band means and LST was further supported by spectral (reflectance DN values), structural (material, construction pattern), and emissivity information of the object. In this study, the urban areas of KMA characterized by concrete material, rough surface texture, less gap between buildings and old structures were represented by high emissivity and high LST. In industry class, concrete surface, localized heat effects, pollution, and gases were influencing high emissivity and high LST. Due to sparseness, low density of vegetation cover, smooth surface of water bodies and wideness of open spaces were influencing low emissivity and low LST.

5.4 *Sensitivity of built-up clusters to LST*

It has been observed that the NDBI of all four built-up clusters were increased during 1988–2018 (see figure 10). Most prominently, NDBI of high-density built-up clusters was increased significantly over time. It was indicated that high-density built-up zones became denser from time to time. In KMA, the high-density built-up zones were located in the areas of Barabazar, Manik Tala, Shyam Bazar, BBD Bagh, etc. These areas were the CBD zones of Kolkata city and highly dense in nature. Development of business centers, administrative offices, good accessibility, and communication, were made such locations more suitable for settlement and business purposes. These areas were also the oldest part of the city.

Similarly, the NDBI of planned zones were also significantly higher. In our study, planned zones included two major planned areas of KMA: (1) Salt Lake City in North 24 Pargana district, (2) Kalyani Township in Nadia district. Salt Lake City was developed during 1958–1965 to accommodate the burgeoning population of Kolkata, whereas the Kalyani Township was developed in the early 1950s. But over time, these areas were accommodated by a huge population to get social benefits, good accessibility, and a better quality of life. Such an increase in population have made these areas denser over time. Interestingly built-up density of slum pockets was shown dynamic nature. The location of the slum pockets was mainly at Chitpur, Sahid colony, near Paikpara, near Bidhan Nagar Railway station, near the Dumdum market where mostly poor and economically backward population of the city have living. During 1988, NDBI was high in slum pockets of KMA due to the huge population, poor infrastructural development, weak economic reforms that forced people to live in

slums. After 1990, steady economic development took place in KMA and people were transferred to permanent settlements. During 2018, the increasing built-up density of slum pockets was due to the migration of poor working population from surrounding states of Bihar, Jharkhand, and Orissa. The surrounding villages of KMA were going through the process of concretization (transformation from kutcha house to pakka house) of houses in the last 30 years. Several government schemes like Indira Awas Yojana (IAY), Pradhan Mantri Awas Yojana (PMAY), housing for all along with socio-economic reform of villages were made the villages denser in built-up concentration (Ananth 2017; Dasgupta 2017).

Though the density of different built-up clusters has increased over time, no significant relationship has been found between built-up density and LST in the last 30 years. Our results were evident that increasing built-up density does not always accelerate the LST concentration for the respective built-up cluster. The relation between different built-up clusters density and LST were dynamic and insignificant (see figure 10). So, we can assume that, not only increasing built-up density but also the degradation of the local environment, increasing air pollution, reduction in water bodies, changes in urban energy balance patterns were equally responsible for increasing LST and for the development of UHII. From the results, we have observed that the LST of 2010 was low in comparison to 1988, 2000 and 2018. Due to El Niño La Niña events, the LST of 2010 was lower than the rest of the examined years. The overall climate of the Indian subcontinent has greatly influenced by such special climatic phenomena during 2009–2011 (Kim *et al.* 2011).

6. Summary and conclusion

A synergetic investigation between temporal LULC and LST based on three different objectives were done, for the first time. Integrated CA–Markov chain modelling, band means relation to LST and temporal analysis between built-up density and LST have been examined over KMA using non-commercial satellite data. From the present study following summary and recommendations can be addressed:

- In comparison to other similar global cities, KMA also experienced a massive built-up expansion that endorses the increasing trend of LST in this region. Such built-up expansion not only happened during 1988–2018 but also will continue for the upcoming future as suggested by our predicted LULC map.
- Considering the soaring alarm of huge urbanization in 2026, growth management policies (i.e., green belt) need to be adopted that would contain the growth in a sustainable way and also consequently reduce the UHII impact over KMA.
- Reforms will require not only for new urbanization policies but also in new building regulations. New urbanization policies such as green building, rainwater harvesting, rooftops with horticulture based plants, more green parks are required to reduce the impact of UHII on KMA.
- Along with the reforms of urbanization policies, environmental protection and enrichment will need on immediate attention in this region. Social plantation, construction of parks within the core urban areas, less encroachment of eastern wetlands (Ramsar Convention), and no construction on agricultural lands have to be addressed in an urgent manner for a sustainable healthy future of KMA.
- Continuous monitoring of the city's land use, with rational, scientific, and sustainable policies must be adopted in order to regulate the trend of unplanned urban sprawl and increasing LST.
- Unless a radical decentralization policy would be adopted, it is impossible to control the unplanned urbanization process in KMA. Planned satellite towns have to be built to regulate irregular urban expansion.
- In our study, we have found the impact of emissivity on the LULC LST relationship using Landsat data and mono-window algorithm. Other space-borne sensors such as Sentinel-2, MODIS and other LST derivation algorithms (i.e., split-window (SW), single-channel (SC) and multi-angle (MA)) need to be examined to understand the band means and LST relationship on different platforms.
- The study has shown that increasing built-up density did not accelerated the LST of the city. It means that other local and regional environmental factors, anthropogenic factors were also similarly responsible for increasing LST of the KMA region.
- The approach of this study can be performed in future research in other cities of India, where climatic and geographical situations are different from KMA.

Acknowledgements

Special thanks to the US Geological Survey, NASA, and Google earth for providing freely available satellite data. Analyses of the data were supported by the Polish National Research Centre (NCN) within the Project No 2016/21/B/ST10/ 02271. Sincere thanks are given to the anonymous reviewers and members of the editorial team for their comments and suggestions.

References

Al-Ahmadi F S and Hames A S 2009 Comparison of four classification methods to extract land use and land cover from raw satellite images for some remote arid areas, Kingdom of Saudi Arabia; *Earth Sci.* **20(1)** 167–191.

Artis D A and Carnahan W H 1982 Survey of emissivity variability in thermography of urban areas; *Remote Sens. Environ.* **12(4)** 313–329.

Ananth P 2017 Housing for poor and the impact of IAY in rural India: Present context; *Int. J. Humanities Social Sci. Res.* **3(1)** 54–56.

Bardhan R, Bandopadhyay S and Gupta K 2015 Rapid estimation of flood prone zones under data constraint scenario: A fuzzy modelling approach; *Proc. HYDRO 2015 INTERNATIONAL viz 20th International Conference on Hydraulics, Water Resources and River Engineering,* December 2015, IIT Roorkee, India

Bardhan R, Debnath R and Bandopadhyay S 2016 A conceptual model for identifying the risk susceptibility of urban green spaces using geo-spatial techniques; *Model. Earth Syst. Environ.* **2(3)** 144.

Bhatta B 2009 Analysis of urban growth pattern using remote sensing and GIS: a case study of Kolkata, India; *Int. J. Remote Sens.* **30(18)** 4733–4746.

Bhattacharjee S and Ghosh S K 2015 spatio-temporal change modeling of LULC: A semantic kriging approach; *ISPRS Annals.*

Bhatti S S and Tripathi N K 2014 Built-up area extraction using Landsat 8 OLI imagery; *Geosci. Remote Sens.* **51(4)** 445–467.

Bojesen M, Skov-Petersen H and Gylling M 2015 Forecasting the potential of Danish biogas production–spatial representation of Markov chains; *Biomass Bioenergy* **81** 462–472.

Brown D G, Pijanowski B C and Duh J D 2000 Modeling the relationships between land use and land cover on private lands in the Upper Midwest, USA; *J. Environ. Manag.* **59(4)** 247–263.

Campagna M, De Montis A, Isola F, Lai S, Pira C and Zoppi C (eds) 2012 Planning Support Tools: Policy analysis, implementation and evaluation; *Proceedings of the Seventh International Conference on Informatics and Urban and Regional Planning,* INPUT2012 FrancoAngeli.

Chakraborty S, Chowdhury B R, Ghosh S, Sen P K and De U K 2019 Statistical analysis of urban regional pre-monsoon rainfall in and around Kolkata, India; *J. Earth Syst. Sci.* **128(3)** 57.

Chander G, Markham B L and Helder D L 2009 Summary of current radiometric calibration coefficients for Landsat MSS, TM, ETM+, and EO-1 ALI sensors; *Remote Sens. Environ.* **113(5)** 893–903.

Chandler T 1965 *The Climate of London;* W Heffer and Sons Ltd., Cambridge, England.

Chandra S, Sharma D and Dubey S K 2018 Linkage of urban expansion and land surface temperature using geospatial techniques for Jaipur City, India; *Arab. J. Geosci.* **11(2)** 31.

Chen L, Li M, Huang F and Xu S 2013 Relationships of LST to NDBI and NDVI in Wuhan City based on Landsat ETM+ image; In: Image and Signal Processing (CISP); *6th International Congress IEEE* **2** 840–845.

Chen W, Panahi M and Pourghasemi H R 2017a Performance evaluation of GIS-based new ensemble data mining techniques of adaptive neuro-fuzzy inference system (ANFIS) with genetic algorithm (GA), differential evolution (DE), and particle swarm optimization (PSO) for landslide spatial modelling; *Catena* **157** 310–324.

Chen W, Pourghasemi H R, Kornejady A and Zhang N 2017b Landslide spatial modeling: Introducing new ensembles of ANN, MaxEnt, and SVM machine learning techniques; *Geoderm.* **305** 314–327.

Chen X L, Zhao H M, Li P X and Yin Z Y 2006 Remote sensing image-based analysis of the relationship between urban heat island and land use/cover changes; *Remote Sens. Environ.* **104(2)** 133–146.

Cheng T and Adepeju M 2014 Modifiable temporal unit problem (MTUP) and its effect on space-time cluster detection; *PLOS One* **9(6)** pe100465.

Dasgupta A 2017 Unlocking the potential of geospatial data; *Space India* **20** 51.

Behera M, Borate S N, Panda S N, Behera P R and Roy P S 2012 Modelling and analyzing the watershed dynamics using Cellular Automata (CA)–Markov model – A geo-information based approach; *J. Earth Syst. Sci.* **121(4)** 1011–1024.

Drăgut L and Blaschke T 2006 Automated classification of landform elements using object based image analysis; *Geomorphology* **81(3–4)** 330–344.

Du P, Liu P, Xia J, Feng L, Liu S, Tan K and Cheng L 2014 Remote sensing image interpretation for urban environment analysis: methods, system and examples; *Remote Sens. Basel.* **6(10)** 9458–9474.

Erbek F S, Özkan C and Taberner M 2004 Comparison of maximum likelihood classification method with supervised artificial neural network algorithms for land use activities; *Int. J. Remote Sens.* **25(9)** 1733–1748.

ERDAS 2009 *ERDAS Field Guide* ^{TM}*—tutorial Imagine;* Atlanta, Georgia

Foody G M 1992 On the compensation for chance agreement in image classification accuracy assessment; *Photogramm. Eng. Remote Sens.* **58(10)** 1459–1460.

Fu P and Weng Q 2016 A time series analysis of urbanization induced land use and land cover change and its impact on land surface temperature with Landsat imagery; *Remote Sens. Environ.* **175** 205–214.

Ghosh S, Chatterjee N D and Dinda S 2018 Relation between urban biophysical composition and dynamics of land surface temperature in the Kolkata metropolitan area: A GIS and statistical based analysis for sustainable planning; *Model. Earth Syst. Environ.* **5** 307–329.

Ghosh S, Singh P and Kumari M 2014 Assessment of urban sprawl and land use change dynamics, using remote sensing technique: A study of Kolkata and surrounding periphery, WB, India.

Grover A and Singh R B 2015 Analysis of urban heat island (UHI) in relation to normalized difference vegetation index (NDVI): A comparative study of Delhi and Mumbai; *Environments* **2(2)** 125–138.

Guo G, Wu Z, Xiao R, Chen Y, Liu X and Zhang X 2015 Impacts of urban biophysical composition on land surface temperature in urban heat island clusters; *Landsc. Urban Plan.* **135** 1–10.

Hamad R, Balzter H and Kolo K 2018 Predicting land use/land cover changes using a CA–Markov model under two different scenarios; *Sustain.-Basel.* **10(10)** 3421.

Hiremath S, Prabhuraj D K, Lakshmikantha B P and Chakraborty S D 2013 Land use/land cover change analysis of Bangalore Urban District and its impact on land surface temperature; *Indian Society of Geomatics and Indian Society of Remote Sensing, Remote Sensing and GIS for Environment with Special Emphasis on Marine and Coastal Dynamics,* Visakhapatnam.

Honnerová P, Martan J, Veselý Z and Honner M 2017 Method for emissivity measurement of semitransparent coatings at ambient temperature; *Sci. Rep-UK* **7(1)** 1386.

Hu Q, Wu W, Xia T, Yu Q, Yang P, Li Z and Song Q 2013 Exploring the use of Google Earth imagery and object-based methods in land use/cover mapping; *Remote Sens.-Basel.* **5(11)** 6026–6042.

Ibrahim F and Rasul G 2017 Urban land use land cover changes and their effect on land surface temperature: Case study using Dohuk City in the Kurdistan Region of Iraq; *Climate* **5(1)** 13.

James K S 2011 India's demographic change: Opportunities and challenges; *Science* **333(6042)** 576–580.

Jiménez-Muñoz J C and Sobrino J A 2003 A generalized single-channel method for retrieving land surface temperature from remote sensing data; *J. Geophys. Res.-Atmos.* **108** (D22).

Kallvetty S and Bandopadhyay S 2018 Spatial explicit modeling to understand the dynamics of landuse switch using open source satellite data; *Geoplanning J. Geomatics Plann.* **5(1)** 1–22.

Keshtkar H and Voigt W 2016 A spatiotemporal analysis of landscape change using an integrated Markov chain and cellular automata models; *Model. Earth Syst. Environ.* **2(1)** 10.

Kim W, Yeh S W, Kim J H, Kug J S and Kwon M 2011 The unique 2009–2010 El Niño event: A fast phase transition of warm pool El Niño to La Niña; *Geophys. Res. Lett.* **38(15)**.

Kumar P, Husain A, Singh R B and Kumar, M 2018 Impact of land cover change on land surface temperature: A case study of Spiti Valley; *J. Mt. Sci.* **15(8)** 1658–1670.

Li X, Mitra C, Marzen L and Yang Q 2016 Spatial and temporal patterns of wetland cover changes in East Kolkata Wetlands, India from 1972 to 2011; *IJAGR* **7(2)** 1–13.

Lo C P and Quattrochi D A 2003 Land-use and land-cover change, urban heat island phenomenon, and health implications; *Photogramm. Eng. Remote Sens.* **69(9)** 1053–1063.

Lombardo M A 1985 Ilha de Calor Nas Metrópoles: O Exemplo de São Paulo (in Portuguese), (first edn), *Hucitec*, São Paulo, Brazil, p 244.

Lv Z Q and Zhou Q G 2011 Utility of Landsat image in the study of land cover and land surface temperature change; *Proc. Environ. Sci.* **10** 1287–1292.

Luedeling E and Buerkert A 2008 Typology of oases in northern Oman based on Landsat and SRTM imagery and geological survey data; *Remote Sens. Environ.* **112** 1181–1195.

Mallick J, Kant Y and Bharath B D 2008 Estimation of land surface temperature over Delhi using Landsat-7 ETM+; *J. Ind. Geophys. Union* **12(3)** 131–140.

McGee T G 2008 Managing the rural–urban transformation in East Asia in the 21st century; *Sustain. Sci.* **3(1)** 155–167.

Mitra A 2018 Estuarine Pollution in the Lower Gangetic Delta Threats and Management; Springer, Berlin.

Mitra S 2002 Planned urbanisation through public participation: Case of the New Town, Kolkata; *Economic and Political Weekly*, pp. 1048–1054.

Mondal A, Guha S, Lakshmi V, Kundu S, Garg R D and Govil H 2017 Evaluating the NCI technique in land use/land cover change detection using Landsat data; *AGU Fall Meeting Abstracts.*

Monserud R A and Leemans R 1992 Comparing global vegetation maps with the Kappa statistic; *Ecol. Model* **62(4)** 275–293, https://doi.org/10.1016/0304-3800(92)90003-W.

Moulds S, Buytaert W and Mijic A 2018 A spatio-temporal land use and land cover reconstruction for India from 1960–2010; *Scientific Data* **5** 180159.

Mukherjee J 2015 Beyond the urban: Rethinking urban ecology using Kolkata as a case study; *Int. J. Sust. Dev.* **7(2)** 131–146.

Oke T R 1987 *Boundary layer climates* (2nd edn); London: Methuen (**435**p).

Pal S and Ziaul S 2017 Detection of land use and land cover change and land surface temperature in English Bazar urban centre; *Egypt J. Remote Sens. Space Sci.* **20(1)** 125–145.

Qin Z, Karnieli A and Berliner P 2001 A mono-window algorithm for retrieving land surface temperature from Landsat TM data and its application to the Israel–Egypt border region; *Int. J. Remote Sens.* **22(18)** 3719-3746.

Regmi R, Saha S and Balla M 2014 Geospatial analysis of land use land cover change predictive modeling at Phewa Lake Watershed of Nepal; *Int. J. Curr. Eng. Tech.* **4** 2617–2627.

Rinner C and Hussain M 2011 Toronto's urban heat island – Exploring the relationship between land use and surface temperature; *Remote Sens.-Basel.* **3(6)** 1251–1265.

Rose L and Devadas M D 2009 Analysis of land surface temperature and land use/land cover types using remote sensing imagery – a case in Chennai City, India; *The seventh International Conference on Urban Clim*ate, **Vol 29**.

Roy J, Chattopadhyay S, Mukherjee S, Kanjilal M, Samajpati S and Roy S 2004 An economic analysis of demand for water quality: Case of Kolkata; *Econ. Polit. Weekly,* pp. 186–192.

Sadhu S 2015 Identification of urban hot spots in relation to built-up surface and nature of buildings in the Kolkata Municipal Corporation (KMC) area; *TTPP* **451.**

Sahana M, Hong H and Sajjad H 2018 Analyzing urban spatial patterns and trend of urban growth using urban sprawl

matrix: A study on Kolkata urban agglomeration, India; *Sci. Total Environ.* **628-629** 1557–1566, https://doi.org/10.1016/jscitotenv.2018.02.170.

Sang L, Zhang C, Yang J, Zhu D and Yun W 2011 Simulation of land use spatial pattern of towns and villages based on CA-Markov model; *Math. Comput. Model* **54(3–4)** 938–943.

Sarkar S, Parihar S M and Dutta A 2016 Fuzzy risk assessment modelling of East Kolkata wetland area: A remote sensing and GIS based approach; *Environ. Model. Softw.* **75** 105–118.

Sharma P 2017 Urbanisation and air quality: A comparative analysis of Delhi and Kolkata; *Int. J. Emerging Technol.* **8(1)** 324–329.

Sharma R, Chakraborty A and Joshi P K 2015 Geospatial quantification and analysis of environmental changes in urbanizing city of Kolkata (India); *Environ. Monit. Assess.* **187(1)** 4206.

Shen H, Huang L, Zhang L, Wu P and Zeng C 2016 Long-term and fine-scale satellite monitoring of the urban heat island effect by the fusion of multi-temporal and multi-sensor remote sensed data: A 26-year case study of the city of Wuhan in China; *Remote Sens. Environ.* **172** 109–125.

Small C 2006 Comparative analysis of urban reflectance and surface temperature; *Remote Sens. Environ.* **104(2)** 168–189.

Snyder W C, Wan Z, Zhang Y and Feng Y Z 1998 Classification-based emissivity for land surface temperature measurement from space; *Int. J. Remote Sens.* **19(14)** 2753–2774.

Sobrino J A, Jimenez-Munoz J C and Paolini L 2004 Land surface temperature retrieval from Landsat TM 5; *Remote Sens. Environ.* **90(4)** 434–440.

Sun J, Yang J, Zhang C, Yun W and Qu J 2013 Automatic remotely sensed image classification in a grid environment based on the maximum likelihood method; *Math. Comput. Model.* **58(3–4)** 573–581.

Thakkar A K, Desai, V R, Patel A and Potdar M B 2017 Post-classification corrections in improving the classification of land use/land cover of arid region using RS and GIS: The case of Arjuni watershed, Gujarat, India; *Egypt J. Remote Sens. Space Sci.* **20(1)** 79–89.

Thomas H and Laurence H M 2006 Modeling and projecting land-use and land-cover changes with a cellular automaton in considering landscape trajectories: An improvement for simulation of plausible future states; *EARSeL eProc.* **5** 63–76.

Walburg G M M E, Bauer M E, Daughtry C S T and Housley T L 1982 Effects of nitrogen nutrition on the growth, yield, and reflectance characteristics of corn canopies; *Agron. J.* **74(4)** 677–683.

Weng Q, Lu D and Liang B 2006 Urban surface biophysical descriptors and land surface temperature variations; *Photogramm. Eng. Remote Sens.* **72(11)** 1275–1286.

Weng Q, Lu D and Schubring J 2004 Estimation of land surface temperature–vegetation abundance relationship for urban heat island studies; *Remote Sens. Environ.* **89(4)** 467–483.

Xia N, Cheng L and Li M 2019 Mapping urban areas using a combination of remote sensing and geolocation data; *Remote Sens.-Basel.* **11(12)** 1470.

Xiong Y, Huang S, Chen F, Ye H, Wang C and Zhu C 2012 The impacts of rapid urbanization on the thermal environment: A remote sensing study of Guangzhou, South China; *Remote Sens.-Basel.* **4(7)** 2033–2056.

Yap D 1975 Seasonal excess urban energy and the nocturnal heat island – Toronto; *Archiv für Meteorologie, Geophysik und Bioklimatologie* Serie B. **23(1–2)** 69–80.

Yuan D 1997 A simulation comparison of three marginal area estimators for image classification; *Photogramm. Eng. Remote Sens.* **53(4).**

Zha Y, Gao J and Ni S 2003 Use of normalized difference built-up index in automatically mapping urban areas from TM imagery; *Int. J. Remote Sens.* **24(3)** 583–594.

Zhao S, Zhou D, Zhu C, Qu W, Zhao J, Sun Y and Liu S 2015 Rates and patterns of urban expansion in China's 32 major cities over the past three decades; *Landsc. Ecol.* **30(8)** 1541–1559.

Corresponding editor: Amit Kumar Patra